






# ***Ab initio* investigation of the topological Hall effect caused by magnetic skyrmions in Pd/Fe/Ir(111)**

Adamantia Kosma <sup>1,2,\*</sup> Philipp Rüßmann <sup>1,3</sup> Yuriy Mokrousov <sup>1,4</sup> Stefan Blügel <sup>1</sup> and Phivos Mavropoulos <sup>2</sup>

<sup>1</sup>*Peter Grünberg Institut (PGI-1), Forschungszentrum Jülich and JARA, 52425 Jülich, Germany*

<sup>2</sup>*Department of Physics, National and Kapodistrian University of Athens, Panepistimioupolis 15784 Athens, Greece*

<sup>3</sup>*Institute for Theoretical Physics and Astrophysics, University of Würzburg, 97074 Würzburg, Germany*

<sup>4</sup>*Institute of Physics, Johannes Gutenberg-University Mainz, 55128 Mainz, Germany*



(Received 25 October 2024; revised 31 March 2025; accepted 1 April 2025; published 8 May 2025)

We present an *ab initio* computational analysis of the topological Hall effect arising from stable magnetic skyrmions in the Pd/Fe/Ir(111) film using noncollinear spin density functional calculations within the Korringa-Kohn-Rostoker Green function method. The semiclassical Boltzmann transport equation is employed for the resistivity and the Hall angle of the system. We explore the influence of the skyrmion size and the impact of disorder on the topological Hall angle.

DOI: [10.1103/PhysRevB.111.174412](https://doi.org/10.1103/PhysRevB.111.174412)

## **I. INTRODUCTION**

Magnetic skyrmions [1–7] have gained focus in many studies in recent years, as they are exceptionally promising for spintronics applications [8]. In ultrathin magnetic films, magnetic skyrmions are two-dimensional noncollinear magnetic spin textures that are topologically protected at the nanoscale [9], i.e., they cannot be continuously deformed into another spin configuration without overcoming an energy barrier [10]. Additionally, they are confined in space and can move as particles. Magnetic skyrmions can be formed at the interface of ferromagnetic films with heavy metals, as a consequence of the spin-orbit coupling (SOC) of conduction electrons and the broken space inversion symmetry, which promote the chiral symmetry-breaking Dzyaloshinskii-Moriya interaction (DMI) [11,12]. Their special characteristics, as their creation, manipulation by electric currents, and detection, have been demonstrated both experimentally and theoretically, making them ideal candidates for computing applications [8,13–17].

Tunneling and Hall effect methods offer promising prospects for the electrical detection of magnetic skyrmions. Among the former, typically applied in the current-perpendicular-to-plane geometry, in particular the noncollinear magnetoresistance effect [18–21] takes advantage of the noncollinear skyrmion structure affecting the tunneling current between the sample and a scanning tunneling microscope tip. The latter method, which is applied in the current-in-plane geometry and refers to the measured response transverse to an electric current and a perpendicularly applied magnetic field, is the subject of this paper. In brief,

Bloch electrons contributing to a current in a ferromagnet are skew scattered by the chiral spin texture of magnetic skyrmions, resulting in a transverse contribution to the current that is detected as a Hall voltage.

In more detail, the detection of skyrmions relies on the topological Hall effect [22–30] (THE) that results from the noncoplanar magnetization texture of skyrmions. In the limit of large skyrmions, one can adopt a semiclassical view of electron transport, where electrons move adiabatically through a magnetic skyrmion texture by which they gain a Berry phase proportional to the topological charge of the skyrmion, which contributes to an effective magnetic field that causes the transverse response of the electrons. The topological Hall effect is an additional contribution to the ordinary [31] (OHE) and anomalous Hall effects [32] (AHE). The former is attributed to the Lorentz force resulting from an external magnetic field in nonmagnetic metals, while the latter occurs in collinear ferromagnets and results from the interplay between the intrinsic magnetization and spin-orbit coupling. Here the spin-orbit interaction causes an effective magnetic field in the reciprocal space leading to the transverse deflection of the electrons.

Deciphering the Hall transport properties in noncollinear textures remains a formidable challenge. For instance, an experimental separation between the anomalous and topological Hall effects is not trivial, as in chiral magnets and skyrmion hosting heterostructures a sizable spin-orbit interaction is required for the formation of skyrmions. A commonly practiced procedure to measure the topological Hall resistance makes use of the assumption of a linear superposition of all Hall resistances, and thus a linear superposition of spin-orbit and topological contributions. Employing this idea, one determines the topological Hall resistance as the difference of the Hall resistances of the ferromagnetic sample with and without skyrmions [23,33]. The validity of this heuristic assumption has recently been questioned in particular for systems with strong spin-orbit interaction such as heterostructures involving layers of 5d-transition metals like Ir or Pt [34].

\*Contact author: a.kosma@fz-juelich.de

In this work, we focus on the topological Hall effect that arises from stable magnetic skyrmions in a Pd/Fe bilayer on Ir(111). The fcc-Pd/Fe/Ir(111) thin film is a paradigmatic system for atomic-scale skyrmions in ultrathin films. Single Néel-type magnetic skyrmions with a size of about four nanometers in which the magnetization textures winds clockwise from the inside to the outside (helicity  $\pi$ ) were detected in this system for the first time by spin-polarized scanning tunneling microscopy (STM) experiments at about 4 K and an external magnetic field of about 2 T [35–37]. Additionally, this heterostructure has been extensively investigated using density functional theory (DFT) simulations to assess its energetic stability [19,38–41]. Today, we know that Pd can grow in an all face-centered-cubic (fcc) stacking or in an hexagonal-close-packed (hcp) stacking geometry leading to two different skyrmions' radii [20,42]. However, to the best of our knowledge, no *ab initio* simulations have been conducted to study the Hall-type transport properties in this heterostructure.

The conventional approach for the calculation of the topological Hall effect relies on the evaluation of the real-space Berry curvature [25,43] acquired by the electrons following adiabatically a smoothly varying noncoplanar magnetization texture of the skyrmion. Here, we take a different, challenging, and hardly practiced route and compute the electronic structure and the topological Hall effect in skyrmion materials by considering entire nanosized skyrmions embedded in ferromagnets. This may be an important route for small skyrmions subject to a large spin-orbit interaction or DMI. Our simulations are based on noncollinear spin-density functional theory [44] within the full-potential relativistic Korringa-Kohn-Rostoker (KKR) Green function method [45,46]. The DFT calculations are used to determine self-consistently the magnetic texture of the skyrmions, and allow the determination of the scattering rate of spin-polarized Bloch electrons at the skyrmion which then serves as an input to the Boltzmann formalism to investigate the topological Hall effect within a realistic description of the electronic structure imposed by the skyrmion in the fcc-Pd/Fe/Ir(111) system.

The Boltzmann formalism takes into account the elastic electron scattering by the skyrmionic topological magnetic structure. The effect of the noncoplanar magnetization direction is included in the scattering amplitude and scattering rate, although the Berry phase of the magnetization profile is not explicitly calculated. Also included is the scattering by the difference in the potential of the skyrmion with respect to the host (difference in the magnetization modulus, in the spin-orbit coupling, and in the nonmagnetic part of the potential). Even though, by definition, the topological Hall effect is only caused by the noncoplanar magnetization profile, all the above scattering sources contribute to skew scattering and to the Hall angle, and cannot be disentangled in an obvious way.

The above sources also contribute to conventional scattering, and thus to the resistivity. The skyrmion concentration in the Fe film enters only as a multiplicative factor to the scattering rate because the skyrmions are experimentally known to be nucleated at random, thus the electron phase is lost during the multiple scattering among them. In addition, the growth of heterostructures inevitably leads to some degree of

structural and chemical disorder. This is taken into account by an effective mean disorder parameter  $\Gamma$ .

Since the skyrmion is formally considered to be a defect, it gives an extrinsic contribution to the AHE. Our formalism focuses on scattering on the Fermi surface and does not include the ordinary, intrinsic AHE derived from the Berry phase of the band structure and the Fermi sea, even though the band structure calculations include the spin-orbit coupling.

The paper is organized as follows. In Sec. II we present our DFT results on the pristine ferromagnetic film and on the formation of stable magnetic skyrmions in the Fe layer of this film. In Sec. III, we briefly describe the DFT formalism and the methodology for the spin-transport calculations combining the KKR method with the Boltzmann transport equation. In Sec. IV we discuss the transport properties of the system, with emphasis on the dependence of the topological Hall effect on the skyrmion size and on additional disorder. Finally, we summarize our findings and main conclusions in Sec. V.

## II. FORMATION OF STABLE MAGNETIC SKYRMIONS

We start our analysis with the formation of stabilized magnetic skyrmions in the Pd/Fe/Ir(111) heterostructure based on *ab initio* simulations. The system consists of a single atomic layer of ferromagnetic Fe deposited on a metallic Ir(111) substrate and, on top of this, there is an additional atomic layer of magnetically susceptible Pd metal, as depicted in Fig. 1(a). The system is in an fcc(111) stacking geometry. In Fig. 1(b), the crystal structure of the near-surface atomic layers is shown in a top view, i.e., the Pd layer, the Fe layer, and its nearest Ir layer. It is easily seen that there is 120° rotational symmetry and three reflection planes perpendicular to the surface.

First, we show the electronic structure of the fcc-stacked ferromagnetic thin film Pd/Fe/Ir(111) of 36-layer thickness (34 Ir layers as structural model for the Ir substrate, 1 Fe and 1 Pd layer; structural details are given in Sec. III). The magnetization is considered perpendicular to the plane. The high-symmetry points of the surface Brillouin zone are given in Fig. 1(c). The band structure, projected to spin-down states within the Fe layer, is presented along the high-symmetry directions  $\Gamma K$  and  $\Gamma M$  in Figs. 1(d) and 1(e). Since spin-orbit coupling is present, all bands are of mixed spin character. However, the states that are of mainly spin-down character are displayed with a higher intensity. The same holds for the states that are more localized in the Fe layer.

In Fig. 1(d) we observe a Rashba-type asymmetry, i.e.,  $E_k \neq E_{-k}$ , in the  $\Gamma$ - $K$  direction. The asymmetry is not very strong. It is well known and stems from the combined action of the exchange field, spin-orbit coupling, and absence of space inversion at the surface and promotes the Dzyaloshinskii-Moriya interaction, resulting in the formation of stable magnetic skyrmions in this system.

Second, we proceed with the calculations on the skyrmion formation. The skyrmion is formally treated as a single but large defect, embedded within a defined radius in the ferromagnetic system Pd/Fe/Ir(111). The defect consists of the same atoms as the host system, but with the magnetization deviating from the ferromagnetic state. Self-consistent

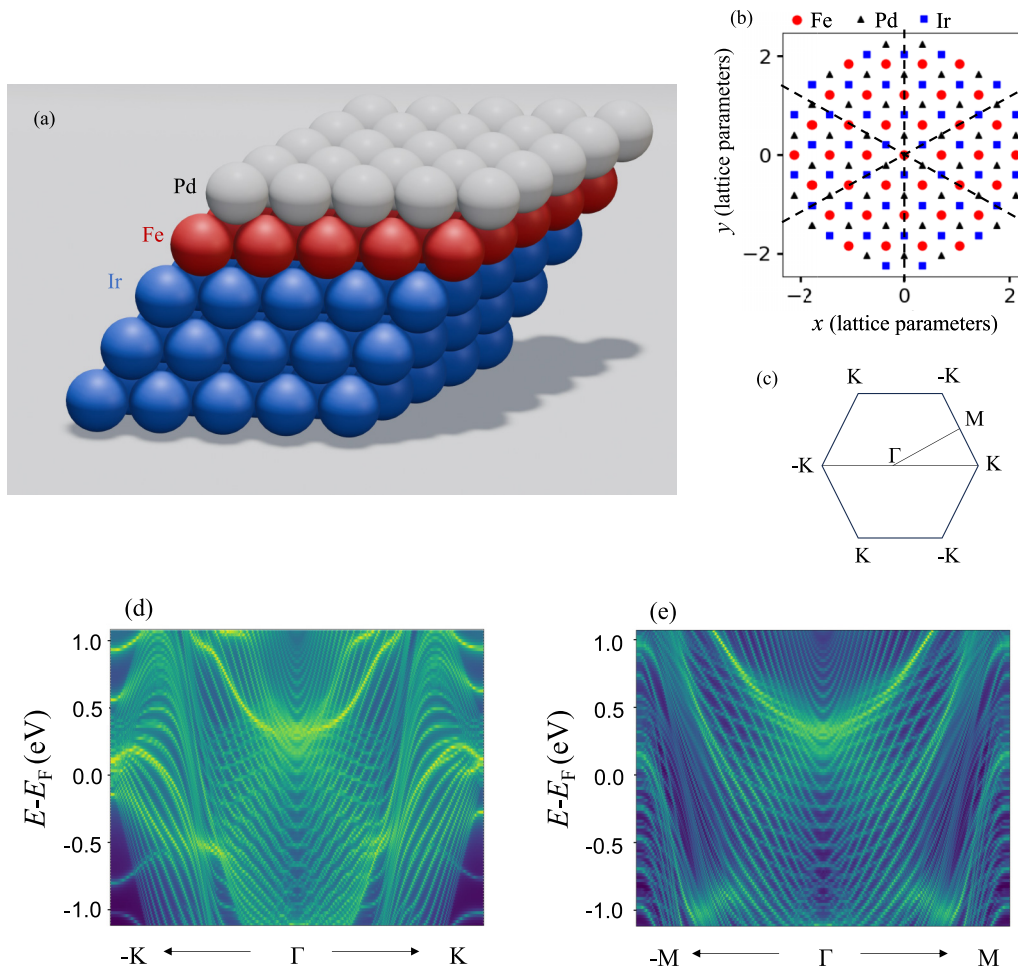


FIG. 1. (a) Illustration of the fcc-stacked Pd/Fe/Ir(111) heterostructure. (b) Top-view illustration of the crystal structure of the near-surface atomic layers. The sites of Fe atoms and their nearest atoms, Pd above and Ir below, are represented by red circles, black triangles, and blue rectangles, respectively. The dashed lines represent the reflection planes perpendicular to the surface. The distance between two consecutive red dots (NN distance) is  $(1/2)\sqrt{2}a$ . The fcc lattice parameter and the NN distance are given in Sec. III A. (c) The Brillouin zone of fcc(111), including the high-symmetry points  $\Gamma$ , K and M. (d) The band structure of a ferromagnetic 36-layer Pd/Fe/Ir(111) film for the spin-down-projected states in the high-symmetry directions (d)  $\Gamma$ K and (e)  $\Gamma$ M. The line intensity corresponds to the degree of localization in the Fe layer.

calculations are performed to achieve the relaxation of the magnetization in the noncollinear skyrmion state. Since we use DFT for the relaxation of the magnetization, the charge density also relaxes, albeit with only a small change with respect to the host charge density. This can lead to the all-electrical detection of skyrmions via the noncollinear magnetic resistance effect in an STM with a nonmagnetic tip [18–21].

While in the experiment the skyrmion radius is controlled by the strength of an external magnetic field, in our calculations this is achieved by the use of the ferromagnetic boundary condition imposed at the Fe atoms of the host film in which the skyrmion is embedded. The skyrmion size is controlled by the number of atoms taken within the defect disk, i.e., by the region where the vector spin density (magnetization), length, and direction of the atomic magnetic moments and charge density are allowed to relax, while being constrained by the boundary conditions. Obviously, one boundary condition is that the atomic potentials outside the defect region are set in the ferromagnetic state with the magnetization perpendicular

to the plane, i.e., the defect disk is considered as being perfectly embedded in a pristine ferromagnetic surface, without periodic boundary conditions. A second boundary condition is set for the central atom, which is spin flipped ( $\theta = 180^\circ$ ) with respect to the ferromagnetic state. The skyrmion is established within the defect disk only, by the self-consistent first-principles relaxation of the magnetization in magnitude and direction, along with the convergence of the atomic potentials. This means that with a sufficiently large disk, the magnetization angle of the atoms at the edge of the disk does not appreciably deviate from the ferromagnetic state. A choice of a smaller disk moves the situation towards a smaller skyrmion, unrelaxed in size, reminiscent of the situation with a strong externally applied magnetic field that leads to smaller skyrmions [36].

In our analysis, we examine two different skyrmion sizes. The smaller skyrmion is formed within a disk comprising 121 sites in the defect region. This includes the first to fifth in-plane neighbors of the central Fe atom, i.e., 37 Fe atoms in total. Additionally, the neighboring atoms of the topmost

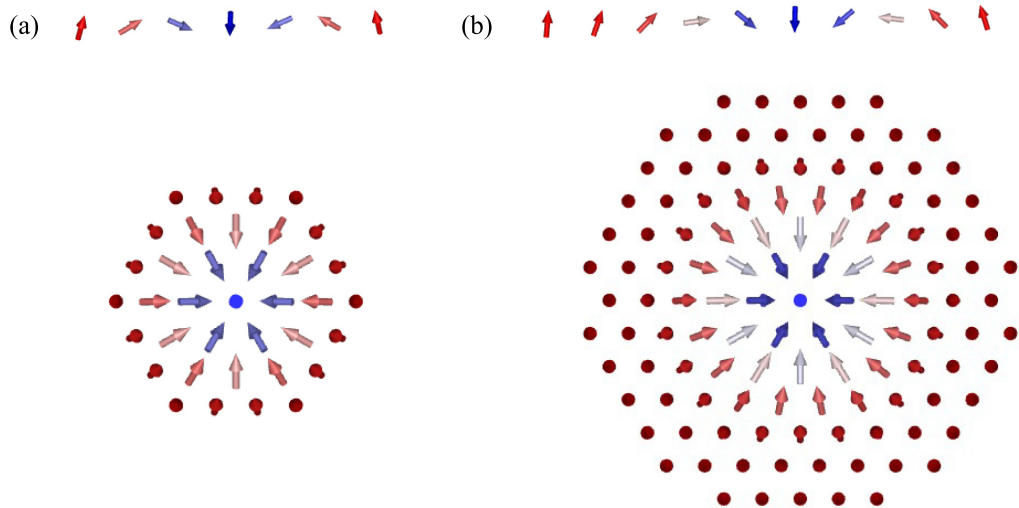


FIG. 2. The relaxed magnetization at the Fe atoms within the two calculated skyrmions in the Pd/Fe/Ir(111) film. The skyrmions include (a) 37 Fe atoms and (b) 121 Fe atoms. The color code stands for the projection of the magnetization in  $z$  direction.

layer of the Ir substrate and of the Pd capping in the skyrmion region, i.e., 42 Ir and 42 Pd atoms are included in the self-consistent calculations. The larger skyrmion profile consists of 349 atoms in the defect region. It includes the 1st to 14th neighbors of the central Fe atom, resulting in 121 Fe atoms in total. This configuration also includes the nearest 114 Ir and 114 Pd atoms.

In Figs. 2(a) and 2(b), we depict the relaxed spin structure for the two different skyrmion sizes. Obviously, both skyrmions are found stable and both have relaxed to a clockwise helicity, in agreement with previous results from the literature [19,35,38]. The corresponding profiles of the magnetization polar angle as function of the distance  $r$  from the center of the skyrmion  $\theta(r)$  are presented in Figs. 2(a), 2(b) (up), and 3. The skyrmion radius is defined as the distance at which the magnetization angle reaches  $90^\circ$ . Thus, we estimate the skyrmion diameter of the smaller skyrmion equal to be  $d_{\text{sk}} = 0.77$  nm, and the larger  $d_{\text{sk}} = 1$  nm. The magnetization at the rim of the smaller skyrmion has relaxed at an angle of approximately  $\theta = 16^\circ$ , while of the larger skyrmion has relaxed at an angle  $\theta = 1.8^\circ$ , very close to the surrounding ferromagnetic state. Consequently, we have successfully achieved the relaxation of magnetization in the case of the larger skyrmion.

The magnetic moments of Fe exchange proximitize also a magnetization of Pd and Ir. We found that Fe imprints the clockwise helicity into the magnetization of Pd and Ir, i.e., the magnetic spin moments follow ferromagnetically polarized the magnetic spin moments of Fe. Since the exchange susceptibility of the Pd toplayer is larger than that of the Ir interface, the induced magnetic moments of Pd are much larger than those of Ir. The induced Ir moments are that small that we report here only on the average magnetic moment of the Ir layer interfacing Fe. The computed spin magnetic moment ( $m_s$ ) of the near-surface layers of Ir, Fe, and Pd are presented in Table I. We find that the calculated spin magnetic moment of the Fe atoms in the ferromagnetic background is large, while the induced magnetic moment of Pd is also non-negligible. Within the skyrmion region, the modulus of the

spin magnetic moments of the Fe atoms ranges from  $2.47 \mu_B$  to  $2.52 \mu_B$  for the small skyrmion of diameter  $d_{\text{sk}} = 0.77$  nm, and from  $2.49 \mu_B$  to  $2.53 \mu_B$  for the large skyrmion of diameter  $d_{\text{sk}} = 1$  nm. Concerning Pd, the spin magnetic moment modulus ranges from  $0.15 \mu_B$  to  $0.27 \mu_B$  for the small skyrmion and from  $0.19 \mu_B$  to  $0.28 \mu_B$  for the large skyrmion.

### III. METHODOLOGY

#### A. Computational details

The host system Pd/Fe/Ir(111) is modeled as a thin film consisting of 36 atomic layers in total, with 34 layers of Ir, 1 layer of Fe, and 1 layer of Pd in the fcc(111) stacking geometry. The configuration is completed by 3 vacuum layers on each side of the film. The fcc lattice constant used for

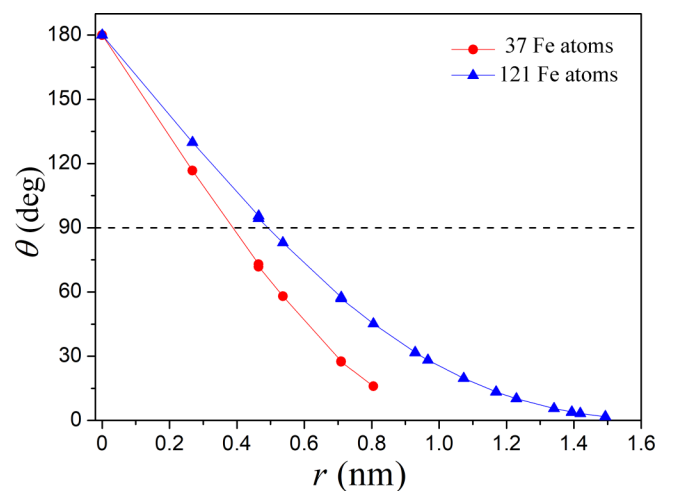


FIG. 3. The profile of the polar angle of the magnetization  $\theta$  as a function of the distance  $r$  from the skyrmion center for the two calculated skyrmions. The red circles and blue triangles represent the skyrmions of 37 and 121 Fe atoms, respectively. The distance at which  $\theta = 90^\circ$  is defined as the skyrmion radius  $r_{\text{sk}} = 0.385$  nm for the small skyrmion and  $r_{\text{sk}} = 0.5$  nm for the large skyrmion.



TABLE I. Calculated spin magnetic moment  $m_s$  in the ferromagnetic state of Pd/Fe/Ir(111) for the topmost atomic layer of Ir, Fe, and Pd.

|              | Ir   | Fe   | Pd   |
|--------------|------|------|------|
| $m_s(\mu_B)$ | 0.04 | 2.53 | 0.29 |

the calculations is  $a = 3.793 \text{ \AA}$ , corresponding to an in-plane nearest-neighbor (NN) distance of  $2.682 \text{ \AA}$ . The interlayer distances are  $d_{\text{Ir-Ir}} = 2.19 \text{ \AA}$ ,  $d_{\text{Fe-Ir}} = 2.06 \text{ \AA}$ ,  $d_{\text{Pd-Fe}} = 2.02 \text{ \AA}$ . All lattice parameters were taken from the work of Dupé *et al.* [38], who *ab initio* structurally optimized the parameters using lattice relaxations.

We employ density functional theory within the local density approximation (LDA) [47,48], utilizing the full-potential relativistic Korringa-Kohn-Rostoker (KKR) Green function method [45,46] as implemented in the Jülich full potential relativistic KKR code [49,50]. The self-consistent solution of the Green function includes the spin-orbit coupling as well as scalar relativistic corrections. For the computation of the Green functions a finite angular momentum cutoff of  $l_{\text{max}} = 2$  was used, which results in matrices of rank  $N_{\text{atom}} \times 2(l_{\text{max}} + 1)^2 = 6282$  for the solution of the Dyson equation at each point in the energy integration contour (here,  $N_{\text{atom}} = 349$  is the number of sites in the defect cluster). For the self-consistent calculations 35 energy points were used. The noncollinear DFT calculations for the self-consistent potential of the skyrmion atoms were carried out with the Jülich KKR impurity-embedding code KKRIMP [51].

The Fermi surface, the group velocity at the Fermi surface, the Boltzmann formalism, and the spin-transport calculations were carried out using the PKKPRIME code [49,52,53]. We use 41 700  $k$  points on the full two-dimensional Fermi surface (Fermi line) of the Pd/Fe/Ir film. Here, for computational time reasons, the film thickness is restricted to 23 layers in total, i.e., 17 Ir atomic layers, 1 Fe layer, 1 Pd layer, and 2 vacuum layers at each surface.

### B. Self-consistent calculations of skyrmions

The charge and spin density within the skyrmion region are found in terms of the space-diagonal part of the Green function  $G^{\text{Sk}}(\mathbf{r}, \mathbf{r}'; E)$  at  $\mathbf{r} = \mathbf{r}'$ , which involves the solution of the Dyson equation

$$G^{\text{Sk}}(\mathbf{r}, \mathbf{r}'; E) = G^{\text{host}}(\mathbf{r}, \mathbf{r}'; E) + \int G^{\text{host}}(\mathbf{r}, \mathbf{r}''; E) \Delta V(\mathbf{r}'') \times G^{\text{Sk}}(\mathbf{r}'', \mathbf{r}'; E) d^3 r''. \quad (1)$$

This equation relates the Green function of the ferromagnetic host system  $G^{\text{host}}$  to the Green function of the perturbed noncollinear system  $G^{\text{Sk}}$  through a perturbing potential  $\Delta V$ . Since the potential difference  $\Delta V$ , as well as the difference in charge and spin density, are confined in the skyrmion region, the integration in the Dyson equation and the sought-for Green function  $G^{\text{Sk}}(\mathbf{r}, \mathbf{r}'; E)$  are also confined in this region. Following the KKR formalism, the Dyson equation is transformed into a linear inhomogeneous system of algebraic equations and solved for  $E$  on a contour in the complex energy

plane.  $G^{\text{Sk}}$ ,  $G^{\text{host}}$ , and  $\Delta V$  are matrices in spin space since we face a noncollinear magnetic problem.

$\Delta V$  is the difference of the potential in response to the rotation of the magnetization. Consequently, it is related to the difference between the magnetization of the skyrmion and the magnetization in the ferromagnetic state. In a first approximation, it reads for the  $i$ -th atom

$$\Delta V_i(\mathbf{r}) \approx B_i(\mathbf{r}) (\hat{\mathbf{e}}_{\mathbf{M}_i} \cdot \boldsymbol{\sigma} - \hat{\mathbf{e}}_z \cdot \boldsymbol{\sigma}), \quad (2)$$

with  $B_i$  the difference of the spin-up and -down components of the potential in the ferromagnetic state, i.e.,  $B_i(\mathbf{r}) = V_i^\uparrow(\mathbf{r}) - V_i^\downarrow(\mathbf{r})$ , and  $\boldsymbol{\sigma} = (\sigma_x, \sigma_y, \sigma_z)$  the Pauli vector, where spin up and spin down are taken with respect to the local spin axis. However, after full relaxation, the potential entails a change with respect to the ferromagnetic state also in  $B_i(\mathbf{r})$  and in the scalar potential  $\frac{1}{2}[V_i^\uparrow(\mathbf{r}) + V_i^\downarrow(\mathbf{r})]$ . The directions  $\hat{\mathbf{e}}_{\mathbf{M}_i}$  are found self-consistently, but respect the boundary condition of being opposite to the direction of the ferromagnetic magnetization ( $\theta = 180^\circ$ ) for the atom in the center and parallel to the ferromagnetic magnetization ( $\theta = 0$ ) for the atoms outside the skyrmion rim. In the noncollinear magnetic skyrmion state, we adopted the approximation that the spin part of the potential,  $B_i(\mathbf{r}) \hat{\mathbf{e}}_{\mathbf{M}_i} \cdot \boldsymbol{\sigma}$ , is collinear within the atomic cell  $i$ , but the direction  $\hat{\mathbf{e}}_{\mathbf{M}_i}$  varies between different atomic cells.

### C. Topological Hall effect calculations

Following previous work [54–57], we proceed with the Boltzmann transport equation approach. The transition matrix  $T$  describing the scattering of a given Bloch state  $\psi_{\mathbf{k}'}$  in the unperturbed ferromagnetic host heterostructure to a final state  $\psi_{\mathbf{k}}$  is given by the matrix elements

$$T_{\mathbf{k}\mathbf{k}'} = \int \psi_{\mathbf{k}}^\dagger(\mathbf{r}) \Delta V(\mathbf{r}) \psi_{\mathbf{k}'}^{\text{Sk}}(\mathbf{r}) d^3 r, \quad (3)$$

where the state scattered by the skyrmion obeys the Lippmann-Schwinger equation

$$\begin{aligned} \psi_{\mathbf{k}'}^{\text{Sk}}(\mathbf{r}) &= \psi_{\mathbf{k}'}(\mathbf{r}) + \int G^{\text{host}}(\mathbf{r}, \mathbf{r}'; E_{\mathbf{k}'}) \Delta V(\mathbf{r}') \psi_{\mathbf{k}'}^{\text{Sk}}(\mathbf{r}') d^3 r' \\ &= \psi_{\mathbf{k}'}(\mathbf{r}) + \int G^{\text{Sk}}(\mathbf{r}, \mathbf{r}'; E_{\mathbf{k}'}) \Delta V(\mathbf{r}') \psi_{\mathbf{k}'}(\mathbf{r}') d^3 r', \end{aligned} \quad (4)$$

and where the region of integration is restricted to the skyrmion defect. Since the full Green function enters in the expression for  $\psi_{\mathbf{k}'}^{\text{Sk}}$ , Eq. (3) expresses the full  $T$  matrix, which is equivalent to summing up all multiple scattering events among the skyrmion atoms to all orders of perturbation theory. For the scattering rate off a single skyrmion,  $w_{\mathbf{k}\mathbf{k}'}$ , we employ the golden rule

$$w_{\mathbf{k}\mathbf{k}'} = \frac{2\pi}{\hbar} \delta(E_{\mathbf{k}} - E_{\mathbf{k}'}) |T_{\mathbf{k}\mathbf{k}'}|^2. \quad (5)$$

In a next step, the semiclassical linearized Boltzmann transport equation is solved self-consistently. This provides the vector mean-free path  $\boldsymbol{\Lambda}_{\mathbf{k}}$  on the Fermi surface:

$$\boldsymbol{\Lambda}_{\mathbf{k}} \cdot \hat{\mathbf{n}}_{\mathcal{E}} = \tau_{\mathbf{k}} \left[ \mathbf{v}_{\mathbf{k}} \cdot \hat{\mathbf{n}}_{\mathcal{E}} + \sum_{\mathbf{k}'} w_{\mathbf{k}\mathbf{k}'} (\boldsymbol{\Lambda}_{\mathbf{k}'} \cdot \hat{\mathbf{n}}_{\mathcal{E}}) \right]. \quad (6)$$

Here,  $\mathbf{v}_k$  represents the group velocity,  $\hat{n}_\mathcal{E} = \mathcal{E}/|\mathcal{E}|$  is the direction of the electric field  $\mathcal{E}$ , and  $\tau_k$  is the relaxation time, defined as

$$\tau_k = 1 / \sum_{k'} w_{kk'}. \quad (7)$$

The Boltzmann equation is self-consistently solved beyond the relaxation time approximation, and it includes the “scattering-in term,” accounting for the vertex corrections [55,58].

The focus of this work is on the investigation of the topological Hall effect. In order to calculate the Hall angle and analyze the topological Hall effect, it is essential to compute the conductivity tensor, which is expressed in terms of the vector mean-free path via the Fermi surface (FS) integral

$$\sigma_{ij} = \frac{e^2}{4\pi^2} \int_{\text{FS}} \frac{dk}{\hbar|\mathbf{v}_k|} (\mathbf{v}_k)_i (\boldsymbol{\Lambda}_k)_j, \quad (8)$$

with  $i$  and  $j \in \{x, y\}$ . As a result, we are able to calculate the resistivity tensor  $\boldsymbol{\rho} = \boldsymbol{\sigma}^{-1}$ . We can now also determine the Hall angle, denoted as  $\alpha = \sigma_{xy}/\sigma_{yy}$ , or, in terms of the resistivity,  $\alpha \approx \rho_{yx}/\rho_{xx}$  when considering  $\sigma_{xy} = -\sigma_{yx}$  and assuming to a good approximation  $\sigma_{xx} = \sigma_{yy}$  because the highly isotropic nature of the  $C_{3v}$  point symmetry of the system, assuming that the electric field is in the  $y$  direction perpendicular to the surface normal in the Pd/Fe/Ir heterostructure. Within this approach, the scattering among different skyrmions is only taken into account on the average by introducing a skyrmion concentration parameter  $c_{\text{Sk}}$  that multiplies the scattering rate  $w_{kk'} \rightarrow c_{\text{Sk}} w_{kk'}$ . The inverse mean-free path and the inverse conductivity tensor scale linearly with the concentration, thus, the concentration cancels in the expression for  $\alpha$ .

#### D. Disorder-induced scattering

In a realistic situation, there are scattering sources aside from the skyrmions, e.g., impurity atoms, structural defects, phonons, thermal fluctuations, etc., that are not precisely known but affect the transport properties. The latter two scattering sources are not so important for this study as the experiments are carried out at 4 K. It is important to consider this residual scattering since otherwise the substrate will show no resistance, causing a short circuit.

A simple way to account for such disorder is by introducing an *ad hoc* scattering rate [59]. The relaxation time  $\tau_k$  [Eq. (7)] is adjusted to  $\tilde{\tau}_k$  with the following relation:

$$\frac{1}{\tilde{\tau}_k} = c_{\text{Sk}} \frac{1}{\tau_k} + \frac{2\Gamma}{\hbar}. \quad (9)$$

Here, the parameter  $\Gamma$  denotes the disorder strength with energy dimensions of the order of meV. Consequently, the matrix elements of the scattering rate  $w_{kk'}$  are modified to ensure the consistency of  $\tilde{\tau}_k = 1 / \sum_{k'} \tilde{w}_{kk'}$ . The adjusted scattering rate  $\tilde{w}_{kk'}$  is determined using the equation [59]

$$\tilde{w}_{kk'} = c_{\text{Sk}} w_{kk'} + \frac{2\Gamma}{\hbar n(E_k)} \delta(E_k - E_{k'}), \quad (10)$$

where  $n(E)$  is the density of states.

Subsequently, the Boltzmann equation [Eq. (6)] is solved, taking into account the constant energy term via the modified relaxation time  $\tilde{\tau}_k$  and the adjusted scattering rate  $\tilde{w}_{kk'}$ .

## IV. RESULTS AND DISCUSSION

In the transport calculations, we consider three different cases as numerical experiments:

- (1) the case of a small skyrmion of 37 Fe atoms,
- (2) the case of a large skyrmion of 121 Fe atoms, but taking into account the electron scattering only by the perturbed potential of the Fe atoms, and
- (3) the full case of a large skyrmion of 121 Fe atoms, taking into account the electron scattering also by the perturbed potential of the Ir substrate and Pd capping in the skyrmion region; this case actually corresponds to our best approximation to a fully relaxed skyrmion magnetization.

As a numerical experiment, our calculations include five different skyrmion concentrations (0.1%, 2%, 4%, 6%, and 10%) in the Pd/Fe/Ir surface. It should be noted that, among these concentrations, the only realistically attainable one is the lowest, 0.1%. Since a skyrmion encompasses a number of the order of 100 Fe atoms (121 atoms, in our calculation of the skyrmion with 1-nm diameter), a 1% concentration already corresponds to full coverage, as one has, e.g., in the case of skyrmion lattice in the Fe/Ir(111) system [12]. Consequently, higher concentrations serve as a check for the consistency of our calculations.

#### A. Relaxation rate

We start with a discussion of the scattering properties. Figure 4 shows the relaxation rate  $1/\tau_k = \sum_{k'} w_{kk'}$  [see Eq. (7)] in a color scale for the states at  $E_k = E_F$ , for the full case (iii) of the large skyrmion. In the left panel, the relaxation rate is shown for the case without disorder, i.e.,  $\Gamma = 0$ , while, in the right panel,  $\Gamma = 0.86$  meV is taken, resulting in an obvious increase of the relaxation rate overall. We see that certain parts of the Fermi surface are rather pronounced in scattering intensity (redshifted regions). These regions correspond to states that are strongly scattered by the skyrmions, hence they must have a high degree of localization near the surface. This hypothesis is tested in Fig. 5, which depicts the wave-function localization  $|\psi_k(\mathbf{r})|^2$  in each atomic layer in the Pd/Fe/Ir(111) system, for a chosen  $\mathbf{k}$  point within a region of high scattering intensity (shown in the inset of Fig. 5). The peak in the Fe layer, and the high degree of localization in the Pd and Ir surface layers, reveal a surface resonance.

#### B. Longitudinal resistivity

We now examine the impact of the disorder strength  $\Gamma$  [Eq. (9)] on the longitudinal resistivity  $\rho_{xx}$ . The results of our calculations are shown in Figs. 6(a) and 6(b) for the smaller and larger skyrmion systems considering the electron scattering only by the Fe atoms within the skyrmion, i.e., cases (i) and (ii), respectively. Since we have two sources of scattering, the skyrmions and the disorder  $\Gamma$ , we expect that some resistivity will survive at  $\Gamma = 0$ , which henceforth we call residual resistivity.

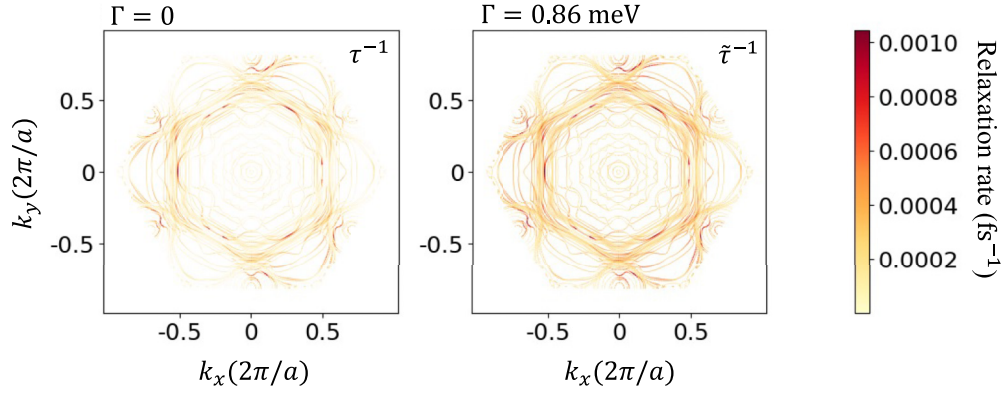


FIG. 4. The relaxation rate  $\tau_k^{-1}$  [Eq. (7)] for the states at the Fermi surface, for the full case of the large skyrmion (case iii). The left panel represents the case without disorder, while the right panel depicts the case with a disorder strength of  $\Gamma = 0.86$  meV.

We observe that in the case of a realistic scenario with 0.1% skyrmion concentration in the surface, the longitudinal resistivity  $\rho_{xx}$  exhibits a linear dependence on the disorder. Here, the skyrmion-induced scattering is very low, so that the skyrmion contribution to the residual resistivity is below point thickness in the plot. However, at higher skyrmion concentrations, the skyrmion contribution to the residual resistivity is apparent. At these concentrations we find that the resistivity as a function of  $\Gamma$  changes slope as  $\Gamma$  increases from zero, but the slope is then stabilized, at higher  $\Gamma$ , as disorder becomes the main source of scattering.

Comparing the two different skyrmion sizes, we see that the residual resistivity is different, but is of the same order of magnitude. This is expected, as the larger skyrmion produces more scattering.

### C. Hall angle

Next, we discuss our results on the Hall angle. The calculated values comprise the contributions of (i) the extrinsic anomalous Hall effect as it arises from impurity skew scattering in a ferromagnetic host, (ii) the spin-orbit interaction of the noncollinear skyrmion texture in difference to the

ferromagnetic state, which gives rise to the anomalous Hall effect, (iii) as well as the topological Hall effect, as expected from the fact that the impurity here (full skyrmion) has a noncoplanar spin texture. The formalism includes all contributions (i)–(iii) and, similar to the experiment, cannot distinguish between them. However, it is clear that the main source of scattering by a skyrmion is its spin texture, while the scattering due to the difference in charge density or spin-orbit coupling compared to the pristine ferromagnetic surface will be comparably insignificant. Therefore, we consider the calculated Hall effect to be a topological Hall effect, at least in the limit of low disorder ( $\Gamma \rightarrow 0$ ) and low spin-orbit interaction.

The behavior of the Hall angle  $\alpha$  as a function of  $\Gamma$  is illustrated in Fig. 6(c) for the two different-sized skyrmion systems (i) and (ii). Here, we present the results only for the realistic skyrmion concentration of 0.1%. While the longitudinal resistivity is of the same order of magnitude for the two skyrmion sizes, a significant increase in the Hall angle in the larger skyrmion system is observed at low  $\Gamma$ . The latter suggests a significant contribution from the off-diagonal conductivity term. We also see that the Hall angle becomes relatively small as the disorder strength increases.

We now discuss case (iii), i.e., the large skyrmion including the contributions of the neighboring atoms of the topmost Ir layer and of the Pd capping layer in the scattering calculations. The results are shown in Fig. 7 (black squares). We observe a significant increase in the calculated Hall angle, as compared to the corresponding results obtained when only the Fe atoms in the skyrmion region are considered during the scattering process [Fig. 7 (red circles)]. We also examine the cases where the electron scattering is considered only by the perturbed potential of the topmost Ir and Fe atoms [Fig. 7 (pink down triangles)], or only by the perturbed potential of the Pd and Fe atoms [Fig. 7 (blue up triangles)]. We find that the contribution of Ir is more significant than that of Pd to the topological Hall angle, likely due to the strong spin-orbit coupling of the Ir substrate. We conclude that the layers with high spin susceptibility, Ir and Pd, are polarized by Fe, contribute to the spin texture, and thus play a significant role in the Hall effect.

In this improved model, the decrease of the Hall angle as a function of the disorder parameter is also seen. This result underscores the significant impact of the degree of disorder in the sample on the measured Hall angle. Therefore, the

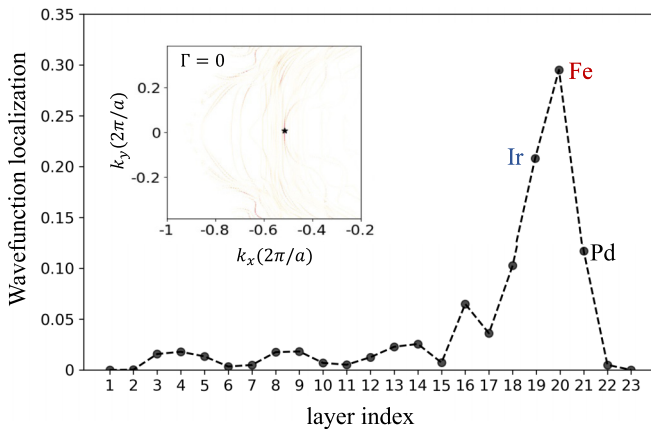


FIG. 5. The wave-function localization in the atomic layers of the Pd/Fe/Ir(111) film, for a  $k$  point in a region with high scattering intensity [ $k = (-0.514, 0) 2\pi/a$ ]. The inset zooms into a region of Fig. 4(a), highlighting the  $k$  point, which is marked with a star.

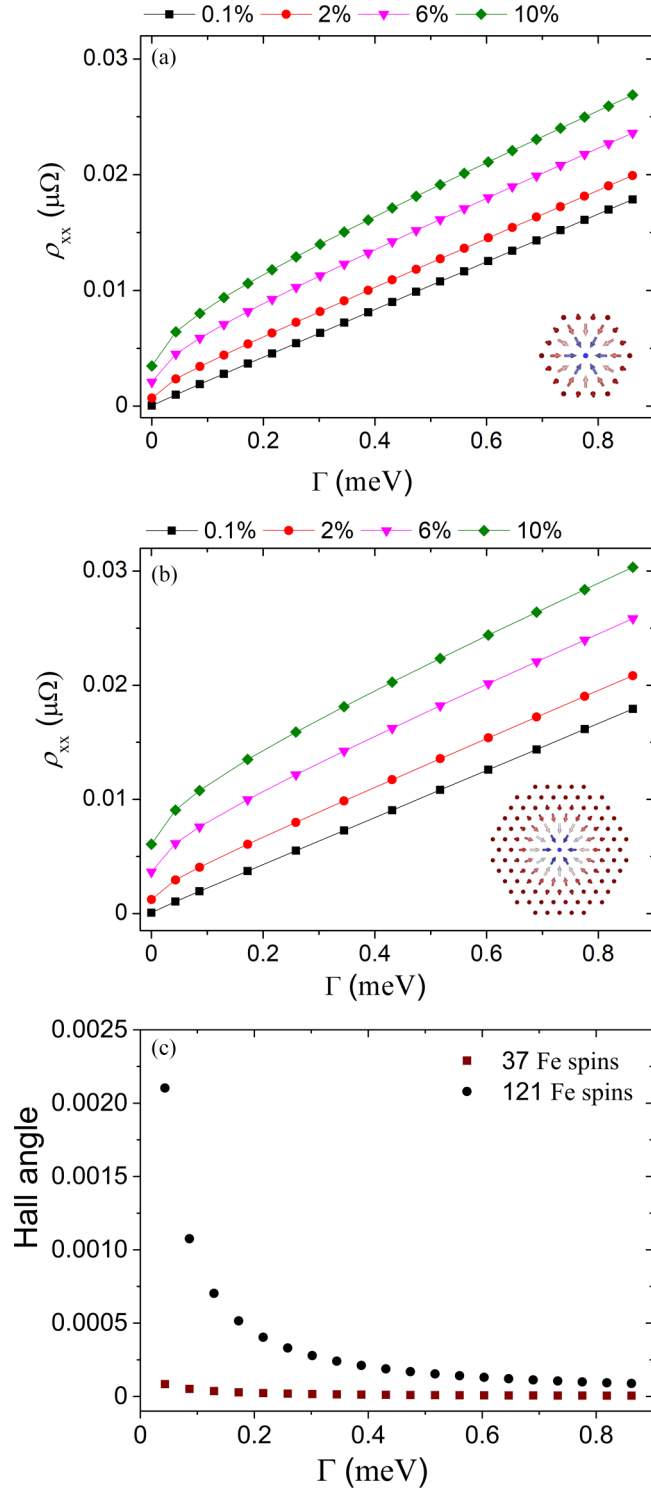


FIG. 6. The longitudinal resistivity  $\rho_{xx}$  as a function of the disorder parameter  $\Gamma$  for the skyrmion of diameter (a) 0.77 nm [case (i)] and (b) 0.99 nm [case (ii)] in Pd/Fe/Ir(111) film. The black squares, red circles, pink down triangles, and green rhombi correspond to four distinct skyrmion concentrations, 0.1%, 2%, 6%, and 10% in the Pd/Fe/Ir(111) film, respectively. (c) The topological Hall angle as a function of  $\Gamma$  for the skyrmions of diameter 0.77 nm [case (i)] and 1 nm [case (ii)] in Pd/Fe/Ir(111) film, considering a 0.1% skyrmion concentration in the system surface.

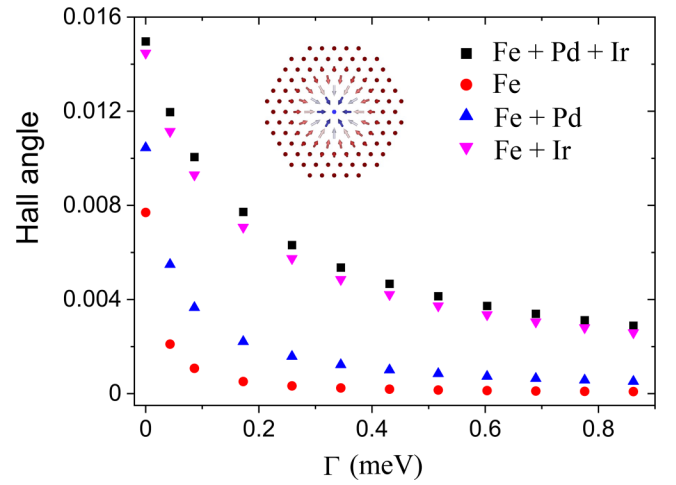


FIG. 7. The topological Hall angle as a function of the disorder parameter  $\Gamma$  for the skyrmion of a diameter of 1 nm and a concentration of 0.1% in the Pd/Fe/Ir(111) surface. The black squares correspond to calculations that take into account the perturbed potential of the Ir substrate and Pd capping in the skyrmion region [case (iii)]. The red circles represent the case where only the perturbed potential of the Fe atoms is considered [as in Fig. 6(c)]. The blue up triangles correspond to the case where only the perturbed potential of the Pd capping and Fe atoms is considered, and the pink down triangles represent the case where only the perturbed potential of the Ir substrate and Fe atoms is included.

inclusion of impurity atoms and other scattering sources is crucial for accurately describing the topological Hall effect.

## V. SUMMARY AND CONCLUSIONS

In this work we have taken up the challenge of using *ab initio* theory to shed light onto the understanding of the Hall effect of noncollinear magnetic textures. For this purpose we have chosen the experimentally and theoretically well-studied fcc-Pd/Fe bilayer on Ir(111). It is a system with strong spin-orbit interaction caused by the 5*d*-metal Ir and exhibits small, magnetic nanoscale skyrmions in the Fe film. We deal with the Hall effect by considering the skew scattering of Bloch electrons from a skyrmion perfectly embedded as a single defect in the ferromagnetic film, determining the magnetic and electronic structure of the whole skyrmion self-consistently, and relating the scattering results in the form of scattering rates to mean-free paths and the conductivity tensor employing the Boltzmann equation. The scattering from single atomic defects or other perturbations, which lead to the typical resistances in the longitudinal transport, were phenomenologically taken into account by a constant parameter  $\Gamma$ . Our main focus is on the topological Hall effect (THE), which we discuss in terms of the Hall angle. Although the THE is the main contribution to the Hall effect in skyrmions, in our calculation, similar to the experiment, the Hall effects due to topology and spin-orbit interaction are interwound.

In summary, we applied the full-potential relativistic KKR Green function method within noncollinear spin



density functional calculations to the formation of stable magnetic skyrmions in the Fe ferromagnetic layer of the fcc-Pd/Fe/Ir(111) heterostructure. We modeled the skyrmion by including 37 Fe atoms and 121 Fe atoms self-consistently in the scattering regions. In both cases the skyrmion radius was found to be about 0.5 nm. Subsequently, a calculation of the electron scattering rate off the skyrmions was used as input to the semiclassical Boltzmann equation for the calculation of the resistivity and the topological Hall angle.

Delving into the electron scattering details of the system, we conclude that surface states and surface resonances scatter strongly off the (surface-localized) skyrmions, and are therefore most significant for the transport properties.

We find four important factors that significantly affect the results and therefore should be accounted for in realistic simulations. First, judging from the two different skyrmion sizes that we analyzed, we infer that the skyrmion size plays an important role. Second, one should incorporate in the transport calculations the noncollinear magnetization that is induced to the Ir and Pd layers by the skyrmion state in the Fe layer. Both significantly increase the robustness of the topological Hall angle against disorder. The large spin-orbit interaction of Ir combined with the small spin polarization ( $0.04 \mu_B$ ) is a more important factor than the large spin polarization of Pd ( $0.29 \mu_B$ ). Third, the large contribution of the spin-orbit interaction to the topological Hall angle raises the question

of disentangling the two contributions. This supports the question of whether the disentanglement leads to additional contributions to the Hall effect beyond the AHE and THE, such as the chiral [60] and non-collinear Hall effects [34]. Fourth, disorder suppresses the Hall angle. Thus, the degree of disorder from different sources (e.g., impurity atoms) must not be neglected.

## ACKNOWLEDGMENTS

We would like to thank J. Bouaziz for fruitful discussions. The research work was supported by the Hellenic Foundation for Research and Innovation (HFRI) under the HFRI Ph.D. Fellowship grant (Fellowship No. 1314). We acknowledge support by the German Academic Exchange Service (DAAD) and the EC Research Innovation Action under the H2020 Programme under the Project HPC-EUROPA3 (Grant No. HPC17CTZOF). A.K., P.R., and S.B. acknowledge funding from the Deutsche Forschungsgemeinschaft (DFG) through ML4Q (Grant No. EXC 2004/1 390534769). Y.M. also acknowledges funding under SPP 2137 “Skyrmionics” of the DFG. This work was supported by computational time granted from the Greek Research & Technology Network (GRNET) in the National HPC facility-ARIS-under Project ID No. “pr007039-TopMagX,” and the High Performance Computing Center Stuttgart (HLRS).

- 
- [1] T. H. R. Skyrme and B. F. J. Schonland, A non-linear field theory, *Proc. R. Soc. London A* **260**, 127 (1997).
  - [2] S. Mühlbauer, B. Binz, F. Jonietz, C. Pfleiderer, A. Rosch, A. Neubauer, R. Georgii, and P. Böni, Skyrmion lattice in a chiral magnet, *Science* **323**, 915 (2009).
  - [3] X. Z. Yu, Y. Onose, N. Kanazawa, J. H. Park, J. H. Han, Y. Matsui, N. Nagaosa, and Y. Tokura, Real-space observation of a two-dimensional skyrmion crystal, *Nature (London)* **465**, 901 (2010).
  - [4] K. Everschor-Sitte, J. Masell, R. M. Reeve, and M. Kläui, Perspective: Magnetic skyrmions—Overview of recent progress in an active research field, *J. Appl. Phys.* **124**, 240901 (2018).
  - [5] A. N. Bogdanov and C. Panagopoulos, Physical foundations and basic properties of magnetic skyrmions, *Nat. Rev. Phys.* **2**, 492 (2020).
  - [6] B. Göbel, I. Mertig, and O. A. Tretiakov, Beyond skyrmions: Review and perspectives of alternative magnetic quasiparticles, *Phys. Rep.* **895**, 1 (2021).
  - [7] K. Wang, V. Bheemarasetty, J. Duan, S. Zhou, and G. Xiao, Fundamental physics and applications of skyrmions: A review, *J. Magn. Magn. Mater.* **563**, 169905 (2022).
  - [8] A. Fert, V. Cros, and J. Sampaio, Skyrmions on the track, *Nat. Nanotechnol.* **8**, 152 (2013).
  - [9] N. Nagaosa and Y. Tokura, Topological properties and dynamics of magnetic skyrmions, *Nat. Nanotechnol.* **8**, 899 (2013).
  - [10] S. Rohart, J. Miltat, and A. Thiaville, Path to collapse for an isolated Néel skyrmion, *Phys. Rev. B* **93**, 214412 (2016).
  - [11] A. Crépieux and C. Lacroix, Dzyaloshinsky–Moriya interactions induced by symmetry breaking at a surface, *J. Magn. Magn. Mater.* **182**, 341 (1998).
  - [12] S. Heinze, K. von Bergmann, M. Menzel, J. Brede, A. Kubetzka, R. Wiesendanger, G. Bihlmayer, and S. Blügel, Spontaneous atomic-scale magnetic skyrmion lattice in two dimensions, *Nat. Phys.* **7**, 713 (2011).
  - [13] J. Sampaio, V. Cros, S. Rohart, A. Thiaville, and A. Fert, Nucleation, stability and current-induced motion of isolated magnetic skyrmions in nanostructures, *Nat. Nanotechnol.* **8**, 839 (2013).
  - [14] W. Kang, Y. Huang, C. Zheng, W. Lv, N. Lei, Y. Zhang, X. Zhang, Y. Zhou, and W. Zhao, Voltage controlled magnetic skyrmion motion for racetrack memory, *Sci. Rep.* **6**, 23164 (2016).
  - [15] G. Yu, P. Upadhyaya, Q. Shao, H. Wu, G. Yin, X. Li, C. He, W. Jiang, X. Han, P. K. Amiri, and K. L. Wang, Room-temperature skyrmion shift device for memory application, *Nano Lett.* **17**, 261 (2017).
  - [16] A. Fert, N. Reyren, and V. Cros, Magnetic skyrmions: Advances in physics and potential applications, *Nat. Rev. Mater.* **2**, 17031 (2017).
  - [17] M. Hoffmann, G. P. Müller, C. Melcher, and S. Blügel, Skyrmion-antiskyrmion racetrack memory in rank-one DMI materials, *Front. Phys.* **9**, 769873 (2021).
  - [18] C. Hanneken, F. Otte, A. Kubetzka, B. Dupé, N. Romming, K. von Bergmann, R. Wiesendanger, and S. Heinze, Electrical detection of magnetic skyrmions by tunnelling non-collinear magnetoresistance, *Nat. Nanotechnol.* **10**, 1039 (2015).
  - [19] D. M. Crum, M. Bouhassoune, J. Bouaziz, B. Schweflinghaus, S. Blügel, and S. Lounis, Perpendicular reading of single confined magnetic skyrmions, *Nat. Commun.* **6**, 8541 (2015).
  - [20] A. Kubetzka, C. Hanneken, R. Wiesendanger, and K. von Bergmann, Impact of the skyrmion spin texture on magnetoresistance, *Phys. Rev. B* **95**, 104433 (2017).

- [21] D. Li, S. Haldar, and S. Heinze, Proposal for all-electrical skyrmion detection in van der Waals tunnel junctions, *Nano Lett.* **24**, 2496 (2024).
- [22] P. Bruno, V. K. Dugaev, and M. Taillefumier, Topological Hall effect and Berry phase in magnetic nanostructures, *Phys. Rev. Lett.* **93**, 096806 (2004).
- [23] A. Neubauer, C. Pfleiderer, B. Binz, A. Rosch, R. Ritz, P. G. Niklowitz, and P. Böni, Topological Hall effect in the *A* phase of MnSi, *Phys. Rev. Lett.* **102**, 186602 (2009).
- [24] N. Kanazawa, M. Kubota, A. Tsukazaki, Y. Kozuka, K. S. Takahashi, M. Kawasaki, M. Ichikawa, F. Kagawa, and Y. Tokura, Discretized topological Hall effect emerging from skyrmions in constricted geometry, *Phys. Rev. B* **91**, 041122(R) (2015).
- [25] K. Hamamoto, M. Ezawa, and N. Nagaosa, Quantized topological Hall effect in skyrmion crystal, *Phys. Rev. B* **92**, 115417 (2015).
- [26] B. Göbel, A. Mook, J. Henk, and I. Mertig, Unconventional topological Hall effect in skyrmion crystals caused by the topology of the lattice, *Phys. Rev. B* **95**, 094413 (2017).
- [27] D. Maccariello, W. Legrand, N. Reyren, K. Garcia, K. Bouzehouane, S. Collin, V. Cros, and A. Fert, Electrical detection of single magnetic skyrmions in metallic multilayers at room temperature, *Nat. Nanotechnol.* **13**, 233 (2018).
- [28] K. S. Denisov, I. V. Rozhansky, M. N. Potkina, I. S. Lobanov, E. Lähderanta, and V. M. Uzdin, Topological Hall effect for electron scattering on nanoscale skyrmions in external magnetic field, *Phys. Rev. B* **98**, 214407 (2018).
- [29] H. Ishizuka and N. Nagaosa, Spin chirality induced skew scattering and anomalous Hall effect in chiral magnets, *Sci. Adv.* **4**, eaap9962 (2018).
- [30] N. Verma, Z. Addison, and M. Randeria, Unified theory of the anomalous and topological Hall effects with phase-space Berry curvatures, *Sci. Adv.* **8**, eabq2765 (2022).
- [31] E. H. Hall, On a new action of the magnet on electric currents, *Am. J. Math.* **2**, 287 (1879).
- [32] N. Nagaosa, J. Sinova, S. Onoda, A. H. MacDonald, and N. P. Ong, Anomalous Hall effect, *Rev. Mod. Phys.* **82**, 1539 (2010).
- [33] M. Lee, W. Kang, Y. Onose, Y. Tokura, and N. P. Ong, Unusual Hall effect anomaly in MnSi under pressure, *Phys. Rev. Lett.* **102**, 186601 (2009).
- [34] J. Bouaziz, H. Ishida, S. Lounis, and S. Blügel, Transverse transport in two-dimensional relativistic systems with nontrivial spin textures, *Phys. Rev. Lett.* **126**, 147203 (2021).
- [35] N. Romming, C. Hanneken, M. Menzel, J. E. Bickel, B. Wolter, K. von Bergmann, A. Kubetzka, and R. Wiesendanger, Writing and deleting single magnetic skyrmions, *Science* **341**, 636 (2013).
- [36] N. Romming, A. Kubetzka, C. Hanneken, K. von Bergmann, and R. Wiesendanger, Field-dependent size and shape of single magnetic skyrmions, *Phys. Rev. Lett.* **114**, 177203 (2015).
- [37] A. O. Leonov, T. L. Monchesky, N. Romming, A. Kubetzka, A. N. Bogdanov, and R. Wiesendanger, The properties of isolated chiral skyrmions in thin magnetic films, *New J. Phys.* **18**, 065003 (2016).
- [38] B. Dupé, M. Hoffmann, C. Paillard, and S. Heinze, Tailoring magnetic skyrmions in ultra-thin transition metal films, *Nat. Commun.* **5**, 4030 (2014).
- [39] E. Simon, K. Palotás, L. Rózsa, L. Udvardi, and L. Szunyogh, Formation of magnetic skyrmions with tunable properties in PdFe bilayer deposited on Ir(111), *Phys. Rev. B* **90**, 094410 (2014).
- [40] I. L. Fernandes, J. Bouaziz, S. Blügel, and S. Lounis, Universality of defect-skyrmion interaction profiles, *Nat. Commun.* **9**, 4395 (2018).
- [41] I. L. Fernandes, J. Chico, and S. Lounis, Impurity-dependent gyrotropic motion, deflection and pinning of current-driven ultrasmall skyrmions in PdFe/Ir(111) surface, *J. Phys.: Condens. Matter* **32**, 425802 (2020).
- [42] S. von Malottki, B. Dupé, P. F. Bessarab, A. Delin, and S. Heinze, Enhanced skyrmion stability due to exchange frustration, *Sci. Rep.* **7**, 12299 (2017).
- [43] C. Franz, F. Freimuth, A. Bauer, R. Ritz, C. Schnarr, C. Duvinage, T. Adams, S. Blügel, A. Rosch, Y. Mokrousov, and C. Pfleiderer, Real-space and reciprocal-space Berry phases in the Hall effect of  $\text{Mn}_{1-x}\text{Fe}_x\text{Si}$ , *Phys. Rev. Lett.* **112**, 186601 (2014).
- [44] U. von Barth and L. Hedin, A local exchange-correlation potential for the spin polarized case. I, *J. Phys. C: Solid State Phys.* **5**, 1629 (1972).
- [45] N. Papanikolaou, R. Zeller, and P. H. Dederichs, Conceptual improvements of the KKR method, *J. Phys.: Condens. Matter* **14**, 2799 (2002).
- [46] H. Ebert, D. Ködderitzsch, and J. Minár, Calculating condensed matter properties using the KKR-Green's function method—recent developments and applications, *Rep. Prog. Phys.* **74**, 096501 (2011).
- [47] W. Kohn and L. J. Sham, Self-consistent equations including exchange and correlation effects, *Phys. Rev.* **140**, A1133 (1965).
- [48] S. H. Vosko, L. Wilk, and M. Nusair, Accurate spin-dependent electron liquid correlation energies for local spin density calculations: A critical analysis, *Can. J. Phys.* **58**, 1200 (1980).
- [49] P. Rüßmann, D. Antognini Silva, D. S. G. Bauer, P. Baumeister, P. F. Bornemann, J. Bouaziz, S. Brinker, J. Chico, P. H. Dederichs, B. H. Drittler, F. Dos Santos, M. dos Santos Dias, N. Essing, G. Géranton, I. Klepetsanis, A. Kosma, N. H. Long, S. Lounis, P. Mavropoulos, E. Mendive Tapia *et al.*, JuDFT-team/JuKKR: v3.6, <https://github.com/JuDFTteam/JuKKR>.
- [50] P. Rüßmann, F. Bertoldo, and S. Blügel, The AiiDA-KKR plugin and its application to high-throughput impurity embedding into a topological insulator, *npj Comput. Mater.* **7**, 13 (2021).
- [51] D. S. G. Bauer, Ph.D. thesis, RWTH Aachen University, 2014.
- [52] B. Zimmermann, Ph.D. thesis, RWTH Aachen University, 2020.
- [53] B. Zimmermann, P. Mavropoulos, N. H. Long, C.-R. Gerhorst, S. Blügel, and Y. Mokrousov, Fermi surfaces, spin-mixing parameter, and colossal anisotropy of spin relaxation in transition metals from *ab initio* theory, *Phys. Rev. B* **93**, 144403 (2016).
- [54] I. Mertig, Transport properties of dilute alloys, *Rep. Prog. Phys.* **62**, 237 (1999).
- [55] M. Gradhand, D. V. Fedorov, P. Zahn, and I. Mertig, Extrinsic spin Hall effect from first principles, *Phys. Rev. Lett.* **104**, 186403 (2010).
- [56] N. H. Long, P. Mavropoulos, B. Zimmermann, D. S. G. Bauer, S. Blügel, and Y. Mokrousov, Spin relaxation and spin Hall transport in 5d transition-metal ultrathin films, *Phys. Rev. B* **90**, 064406 (2014).
- [57] A. Kosma, P. Rüßmann, S. Blügel, and P. Mavropoulos, Strong spin-orbit torque effect on magnetic defects due to topological

- surface state electrons in  $\text{Bi}_2\text{Te}_3$ , [Phys. Rev. B \*\*102\*\*, 144424 \(2020\)](#).
- [58] W. H. Butler, Theory of electronic transport in random alloys: Korringa-Kohn-Rostoker coherent-potential approximation, [Phys. Rev. B \*\*31\*\*, 3260 \(1985\)](#).
- [59] G. Géranton, B. Zimmermann, N. H. Long, P. Mavropoulos, S. Blügel, F. Freimuth, and Y. Mokrousov, Spin-orbit torques and spin accumulation in FePt/Pt and Co/Cu thin films from first principles: The role of impurities, [Phys. Rev. B \*\*93\*\*, 224420 \(2016\)](#).
- [60] F. R. Lux, F. Freimuth, S. Blügel, and Y. Mokrousov, Chiral Hall effect in noncollinear magnets from a cyclic cohomology approach, [Phys. Rev. Lett. \*\*124\*\*, 096602 \(2020\)](#).